This is the peer-reviewed, final accepted version for American Mineralogist, published by the Mineralogical Society of America.
The published version is subject to change. Cite as Authors (Year) Title. American Mineralogist, in press.
DOI: https://doi.org/10.2138/am-2021-7843. http://www.minsocam.org/

Effect of structural water on the elasticity of orthopyroxene

Mingqiang Hou[1], Wen-Yi Zhou[1,2], Ming Hao[1,2], Florian Tian-Siang Hua[3], Jennifer Kung[3], Dongzhou Zhang[4,5], Przemyslaw K. Dera[4], Jin S. Zhang[1,2#]

[1]Institute of Meteoritics, University of New Mexico, Albuquerque, NM, USA

[2]Department of Earth and Planetary Sciences, University of New Mexico, Albuquerque, NM, USA

[3]Department of Earth Sciences, National Cheng-Kung University, Tainan, Taiwan

[4]Hawaii Institute of Geophysics and Planetology, School of Ocean and Earth Science and Technology, University of Hawaii at Manoa, Honoluu, HI, USA

[5]Center of Advanced Radiation Source, University of Chicago, Chicago, IL, USA

Corresponding author. Email: jinzhang@unm.edu

Abstract:

As a major nominally anhydrous mineral (NAM) in the Earth's upper mantle, orthopyroxene could host up to several hundred ppm H_2O in its crystal structure and transport the H_2O to the deep Earth. To study the effect of structural H_2O on the elasticity of orthopyroxene, we have measured the single-crystal elasticity of $Mg_{1.991}Al_{0.065}Si_{1.951}O_6$ with 842-900 ppm H_2O and 1.64±0.20 wt.% Al_2O_3 at ambient conditions using Brillouin spectroscopy. The best-fit single-crystal elastic moduli (C_{ij}s), bulk (K_{S0}) and shear (G_0) modulus of the hydrous Al-bearing orthopyroxene were determined as: C_{11}=235(2) GPa, C_{22}=173(2) GPa, C_{33}=222(2) GPa, C_{44}=86(1) GPa, C_{55}=82(1) GPa, C_{66}=82(1) GPa, C_{12}=75(3) GPa, C_{13}=67(2) GPa, and C_{23}=49(2) GPa, K_{S0}=111(2) GPa, and G_0=78(1) GPa. Systematic analysis based on the results presented in this and previous studies suggests that the incorporation of 842-900 ppm H_2O would increase C_{13} by 12.0(7)% and decrease C_{23} by 8.6(8)%. The effects on C_{11}, C_{22}, C_{33}, C_{44}, C_{66}, K_{S0} and V_P are subtle if not negligible when considering the uncertainties. The C_{55}, C_{12}, G_0, and V_S are not affected by the presence of structural H_2O. Although

laboratory experiments show that Fe,Al-bearing orthopyroxenes can host up to 0.8 wt% H_2O in its structure, future high pressure-temperature elasticity measurements on orthopyroxene with higher H_2O content are needed to help better quantify this effect.

Keywords: Elasticity; Orthopyroxene; Structural water; Seismic velocities

1. Introduction

Water, in the form of structural H_2O or free H_2O, is transported into the deep Earth's interior primarily via subduction. As an important carrier of structural H_2O, NAMs contain a small amount of H_2O in the form of hydroxyl as point defects in their crystalline structures (Demouchy and Bolfan-Casanova, 2016; Ni et al., 2017; Ohtani, 2005, 2015; Ohtani et al., 2004). The bonded structural H_2O can reach up to 1.2-3.1wt.% in the experimentally synthesized NAM crystals (Inoue et al., 1995; Kohlstedt et al., 1996). Moreover, a hydrous ringwoodite inclusion containing ~1.5 wt.% H_2O was recently discovered in a natural diamond (Pearson et al., 2014), further highlighting the critical role that NAMs played as a possible major volatile reservoir in the deep Earth. Structural H_2O significantly impacts the ionic diffusion, dislocation motion, electrical conductivity, phase transitions, melting temperature, and viscosity of mantle minerals (Costa and Chakraborty, 2008; Demouchy and Bolfan-Casanova, 2016; Jacobsen et al., 2010; Yoshino et al., 2009; Zhang et al., 2012). In particular, recent studies have suggested that the presence of structural H_2O can result in some observable seismic signatures in the deep Earth (Kong et al., 2020; Van der Meijde et al., 2003; Yuan and Beghein, 2013). Consequently, evaluating the effect of structural H_2O on the elastic properties of NAMs is crucial to understand the seismic structure, volatile recycling, and mantle mineralogy in the deep Earth (e.g. Ni et al., 2017; Ohtani, 2015; Ohtani et al., 2004).

The Earth's pyrolitic upper mantle is primarily composed of olivine, orthopyroxene, clinopyroxene, and garnet. The effects of structural H_2O on the elasticity of olivine and its high-pressure polymorphs have been extensively studied (Buchen et al., 2018; Inoue et al., 1998; Jacobsen et al., 2008; Kavner, 2003; Mao et al., 2008; Mao et al., 2011; Mao et al., 2012; Schulze et al., 2018). It was suggested that the presence of 1 wt.% structural H_2O in the olivine polymorphs could reduce seismic velocities up to ~2.5% (Inoue et al., 1998; Jacobsen et al., 2008; Mao et al., 2008; Mao et al.,

2011; Mao et al., 2012) and enhance the S-wave splitting anisotropy (Inoue et al., 1998; Jacobsen et al., 2008). However, recent studies showed that high pressure would suppress the effect of structural H_2O and the hydration-induced reductions of sound velocities vanish at transition zone pressure-temperature conditions (Buchen et al., 2018; Schulze et al., 2018). Moreover, the effects of structural H_2O on the elastic properties of the Na, Al bearing-clinopyroxene and garnet were found to be negligible at room temperature condition (Fan et al., 2019; Mans et al., 2019). Although the orthorhombic orthopyroxene is the second most abundant mineral in the pyrolitic upper mantle, there has been no report about the effect of structural H_2O on its single-crystal elastic properties to date.

Compared with olivine, H_2O preferably partitions into orthopyroxene at depth above ~300 km in the upper mantle (Demouchy and Bolfan-Casanova, 2016; Sakurai et al., 2014) and the incorporation of Al as chemical impurity enhances this partitioning process (Grant et al., 2006; Rauch and Keppler, 2002; Smyth et al., 2007). There are two substitution mechanisms for structural H_2O in aluminous orthopyroxene. One is $Al^{3+} + H^{+}$ substitution for Si^{4+} and the other is $Al^{3+} + H^{+}$ substitution for 2 Mg^{2+}. Laboratory-synthesized orthopyroxene crystals with high Al_2O_3 content (9-12 wt.%) can host up to ~0.8 wt.% H_2O in its crystal structure (Mierdel et al., 2007), although natural orthopyroxenes commonly show lower H_2O concentration on the level of several hundred to 1000 ppm (Ohtani, 2015; Xu et al., 2018).

Orthopyroxene presents the lowest isotropic aggregate compressional and shear velocities (V_P and V_S) among all major upper mantle minerals, and has been proposed as a candidate to explain the low seismic velocity zones in the upper mantle (Reynard et al., 2010). Single crystal elastic properties of Al, Fe, and Ca-bearing orthopyroxene have been experimentally determined in a wide compositional range (Bass and Weidner, 1984; Chai et al., 1997; Flesch et al., 1998; Jackson et al., 1999, 2007; Perrillat et al., 2007; Picek, 2015; Qian et al., 2018; Reynard et al., 2010; Webb and Jackson, 1993; Zhang et al., 2013; Zhang and Bass, 2016). The incorporation of Fe significantly reduces the elastic moduli of orthopyroxene, whereas Al increases them (Picek, 2015). The incorporation of Ca, on the other hand, slightly decreases the elastic properties of orthopyroxene (Perrillat et al., 2007). In this study, to evaluate the effect of structural H_2O on elastic properties of

orthopyroxene, we conducted single-crystal Brillouin spectroscopy measurements of synthetic Al-bearing orthopyroxene with 842-900 ppm H_2O at ambient conditions.

2. Materials and Methods

Hydrous Al-bearing orthopyroxene crystals were synthesized at 5.5 GPa and 1473 K using a multi-anvil large volume press at National Cheng Kung University. Starting materials were oxide and hydroxide mixtures of SiO_2, MgO, $Mg(OH)_2$, and $Al(OH)_3$. Detailed synthesis method and procedure can be found in Hua et al. (2020). The size of the synthesized crystals ranges from 100 to 200 μm. The chemical composition of the crystals measured in this study was determined using a JEOL 8200 Electron Microprobe at the Institute of Meteoritics at University of New Mexico, operating at 15 kV accelerating voltage and 20 nA beam current. The element standards were olivine for Mg and Si, enstatite oxygen standard for O, and orthoclase for Al. The chemical formula is determined to be $Mg_{1.991}Al_{0.065}Si_{1.951}O_6$ with 39.82(43) wt.% MgO, 58.18(73) wt.% SiO_2, and 1.64(20) wt.% Al_2O_3. The H_2O content was measured by SIMS technique and determined to be 842-900 ppm (Hua et al., 2020).

Three hydrous Al-bearing orthopyroxene crystals, which were examined to be inclusion-free under petrographic microscope, were selected and double-side polished with Al_2O_3 polishing film. The thicknesses of the samples were 18-20 μm. The orientations and unit cell parameters of two samples were determined in the Atlas X-Ray Diffraction Lab at the University of Hawai'i at Manoa and the third one was measured at 13-BM-C, GeoSoilEnviroCARS (GESCARS), Advanced Phonon Source, Argonne National Laboratory. The experimental setup and details can be found in Mans et al. (2019). The face normals of the three polished crystals are (0.940, -0.150, 0.307), (-0.566, 0.675, 0.472), and (-0.099, -0.558, -0.824) referring to the fractional coordinate system for orthopyroxene with unit cell axes a, b, and c as basis vectors. The accuracy of the measured plane normal is better than 0.5˚, which arises from the angular difference between the rotational axis of the DAC sample holder and the incident X-ray beam at the Atlas X-Ray diffraction Lab at University of Hawaii and GSECARS sector13BMC. The unit cell parameters (a=5.175(3) Å, b=8.804(7) Å, c=18.216(3) Å, and V=829.84(83) $Å^3$) were determined by analyzing the X-ray diffraction images from all three

118 samples, and the density was then calculated to be ρ_0=3.218(3) g/cm^3 using the chemical formula
119 and unit cell volume.
120
121 Brillouin spectroscopy measurements were conducted in the high-pressure laser spectroscopy
122 laboratory at the University of New Mexico. A 300 mW single-mode diode-pumped solid state laser
123 with a wavelength (λ_0) of 532 nm was employed as the light source. A Sandercock-type 6-pass
124 tandem Fabry-Pérot interferometer was used for resolving the Brillouin frequency shift. The optical
125 setup of the Brillouin spectroscopy system can be found in Zhang et al. (2015). All the experiments
126 were conducted using a 50˚ symmetric forward scattering geometry. The scattering angle (θ) was
127 calibrated to be 50.77(5)˚ before the experiments by a standard Corning 7980 silica glass, whose
128 velocities have been precisely measured by the GHz ultrasound interferometry (Zhang et al. 2011).
129 The sample crystal was placed on top of the culet of a diamond anvil cell for Brillouin experiments.
130 The tilting and non-parallelism of the sample and the diamond anvil cell are negligible in the
131 experiments. Under cross-polarized illumination of the petrographic microscope, the interference
132 color of the double-side polished crystals is even, suggesting uniform thickness across the crystals.
133 On the other hand, as part of the alignment process, we have also examined the tilting using the
134 laser beam reflected at the diamond cutlets, tables and crystal surfaces with 0˚ incident angle. The
135 reflected laser beams match each other and the incident laser beam nicely, suggesting that the tilting
136 is minimal. We calibrated the free spectral range (FSR) between the FP1 peaks under reflection
137 mode of the interferometer for at least 6 times before and after every experimental run, and the
138 difference is always within 0.5 channels for a total of 1024-channel setup. This propagates to an
139 uncertainty of less than 0.05% of the FSR and thus less than 0.005 km/s for each velocity
140 measurement, which is within the resolution of Brillouin measurements of 0.03 km/s. The v_P and v_S
141 were measured at 13 different χ angles (0˚, 30˚, 60˚, 90˚, 120˚, 150˚, 180˚, 195˚, 225˚, 255˚, 285˚,
142 315˚, 345˚) for all 3 crystals along the 360˚ azimuth. The differences between determined velocities
143 at χ=0˚ and χ=180˚ are within 0.05 km/s, again suggesting minimal geometrical errors in the
144 experiments. The typical collection time for each spectrum is 10 minutes. Figure 1 shows a typical
145 Brillouin spectrum and the signal-to-noise ratios are ~3 and ~7 for v_P and v_S, respectively.
146
147 Under a forward symmetric scattering geometry, the Brillouin shift $\Delta\omega$, which is the difference

between incident laser frequency (ω_i) and scattered light frequency (ω_s), depends on the velocity along the probed phonon direction, the laser wavelength λ_0, and the external experimental angle between the incident and the scattered light θ^* (Speziale et al., 2014; Whitfield et al., 1976; Zhang et al., 2015),

$$\Delta\omega = \omega_i - \omega_s = 2sin\left(\frac{\theta*}{2}\right)\frac{v}{\lambda_0} \quad (1)$$

where v is the speed of the acoustic phonons in the sample.

The nine independent C_{ij}s can be calculated from the obtained phonon direction – v_P – v_S data set by a least-squares inversion of the Christoffel equation (Weidner and Carleton, 1977).

$$\det\left|c_{ijkl}n_j n_l - \rho v^2 \delta_{ik}\right| = 0 \quad (2)$$

where c_{ijkl} is the 4th order elasticity tensor, n_j and n_l are the directional cosines of the wave vector, ρ is density, and δ_{ik} is the Kronecker delta (Musgrave, 1970). The predetermined plane normal by single-crystal X-ray diffraction were fixed during the inversion process. The angular uncertainty of less than 0.5° for the plane normal would result in an uncertainty of less than 0.01 km/s in the measured acoustic velocities, which is well below the Brillouin measurement uncertainty of 0.03 km/s. However, we did refine the actual individual experimental phonon directions. Given a starting C_{ij} model of orthopyroxene (Zhang and Bass, 2016), we calculated a set of phonon directions for each Brillouin measurement after fixing the plane normals. Then based on the phonon direction – v_P – v_S data set, we calculated the best-fit Cij model through a least-square inversion of the Christoffel equation. Afterwards, we then recalculate the phonon directions of each measurement based on this newly obtained best-fit C_{ij} model. The recalculated phonon directions and the velocities were used as the input to calculate an updated C_{ij} model for another round. This process was repeated for 2-3 times until the difference in root-mean-square (RMS) residuals of two successive runs was less than 0.001km/s. The final best fit C_{ij} model we obtained has the RMS error of 0.055 km/s.

3. Results

The best-fit C_{ij}s are: C_{11}=235(2) GPa, C_{22}=173(2) GPa, C_{33}=222(2) GPa, C_{44}=86(1) GPa, C_{55}=82(1)

GPa, C_{66}=82(1) GPa, C_{12}=74(3) GPa, C_{13}=67(2) GPa, and C_{23}=49(2) GPa (Table 1). Figure 2 shows the measured acoustic velocities of the three samples (Supplementary Material Table S1-S3) and the velocities predicted by the best-fit C_{ij} model. If the laboratory geometrical errors are negligible, the velocities of orthopyroxene measured at χ angle along the 360 ° azimuth should be the same as the velocities determined at χ-180°. Figure 2 plots the data measured at χ between 180°-360° together with the data measured below 180°. The internal consistency between the data collected at (0°, 30°, 60°, 90°, 120°, 150°) and (180°, 195°, 225°, 255°, 285°, 315°, 345°) again suggests the minimal geometrical errors in this study. Voigt-Reuss-Hill (VRH) averaging scheme was employed to calculate the K_{S0} and G_0 (Hill, 1963), which yielded 111(2) GPa and 78(1) GPa, respectively. The aggregate V_P and V_S are calculated to be 8.18(3) km/s and 4.94(2) km/s, respectively.

Our study demonstrates that the effects of Al_2O_3 and structural H_2O on the elasticity of orthopyroxene are coupled, and there is no existing study to quantify the contribution of Al_2O_3. The elastic properties of Fe-bearing orthopyroxene with Al_2O_3 content ranging from 0.4-5.0 wt.% have been studied (Chai et al., 1997; Jackson et al., 2007; Webb and Jackson, 1993; Zhang and Bass, 2016). Decoupling the effects of Fe and Al_2O_3 is feasible because the effect of Fe on the elasticity of orthopyroxene within a wide range of Fe# (Fe# $= \frac{[FeO]}{[FeO]+[MgO]}$) from 0-100 had been studied (Picek, 2015). The C_{11}, C_{22}, C_{33}, C_{44}, C_{55}, and C_{66} of Fe-bearing orthopyroxene decrease with Fe#, whereas C_{12}, C_{13}, and C_{23} are insensitive to Fe#. To quantify the Al_2O_3 effect on the elastic properties of orthopyroxene, we would need to firstly evaluate the effect of Fe. Since the Fe# is less than 15 in the Al-bearing orthopyroxene samples studied by Chai et al. (1997), Jackson et al. (2007), and Zhang and Bass (2016), we choose the data with the compositional range of interest for Fe# 0-15 in Picek (2015) together with previous studies (Jackson et al., 1999, 2007) to re-analyze the single-crystal elasticity data of Fe-bearing Al-free orthopyroxene. We found that increasing the Fe# by 1 would decrease C_{11}, C_{22}, C_{33}, C_{44}, C_{55}, and C_{66} by -0.38(15) GPa, -0.48(13) GPa, -0.68(6) GPa, -0.06(1) GPa, 0 GPa, and -0.10(1) GPa, respectively. On the other hand, there is ~1.1 wt.% CaO in the Al,Fe-bearing orthopyroxene samples of Chai et al. (1997) and Zhang and Bass (2016). The effect of Ca on the elasticity of orthopyroxene had been carefully studied and 1.1 wt.% CaO would reduce the C_{11}, C_{22}, C_{33}, C_{44}, C_{55}, C_{66}, C_{12}, C_{13}, and C_{23} by 2.2%, 1.7%, 3.5%, 0.56%, 3.8%, -0.75%,

206 2.1%, 3.4%, and 5.6%, respectively (Jackson et al., 1999; Perrillat et al., 2007).

207

208 After removing the effects of both Fe and Ca, we plotted the single-crystal and aggregate elastic
209 moduli, as well as aggregate velocities of orthopyroxene as a function of Al_2O_3 content in Figure 3
210 (Supplementary Material Table S4). The shaded area describes the effect of Al_2O_3 on the elasticity
211 of orthopyroxene within the 95% confidence interval. The comparison between the data obtained in
212 this study for hydrous Al-bearing orthopyroxene and previous anhydrous Al-bearing orthopyroxene
213 in Figure 3 makes it possible to evaluate the effect of structural H_2O. The C_{11}, C_{22}, C_{33} of the
214 hydrous Al-bearing orthopyroxene are 1.7(2)%, 3.0(1)% and 2.1(4)% lower compared with its
215 anhydrous counterparts, although the difference is subtle considering the experimental uncertainty.
216 On the other hand, the decrease of C_{23} is more significant, up to 8.6(8)%. Interestingly, structural
217 H_2O increases C_{44}, C_{66}, and C_{13} of the Al-bearing orthopyroxene by 2.6(3)%, 4.1(2)%, and 12.0(7)%,
218 respectively. Structural H_2O has negligible effect on C_{55}, C_{12}, Ks_0, G_0 and Vs, although V_P is slightly
219 decreased.

220

221 In addition, we also calculated the universal anisotropy (A^U), azimuthal V_P (A^{Vp}), and radial V_S
222 anisotropy (D^{Vs}) of the hydrous Al-bearing orthopyroxene (Ranganathan and Ostoja-Starzewski,
223 2008). A^U describes the overall elastic anisotropy for materials with arbitrary symmetry and can be
224 calculated as follows,

225 $$A^U = 5\frac{G_V}{G_R} + \frac{K_{S,V}}{K_{S,R}} - 6 \quad (3)$$

226 where G and K_S are the shear and bulk moduli and the subscripts V and R represent Voigt and Reuss
227 bound, respectively. A^{Vp} and D^{Vs} are the maximum v_P difference along different directions and
228 maximum v_S difference between the two orthogonally polarized shear waves propagating along the
229 same direction, respectively.

230 $$A^{V_P} = \frac{v_{P,max} - v_{P,min}}{V_{P_{VRH}}} \quad (4)$$

231 $$D^{V_S} = \frac{|v_{S_1} - v_{S_2}|_{max}}{V_{S_{VRH}}} \quad (5)$$

232 The calculated anisotropy indices are 0.115(10), 0.148(6), and 0.153(6) and presented in Figure 4.
233 With increasing the Al_2O_3, A^U and A^{Vp} decrease, whereas D^{Vs} slightly increases. Compared with the
234 anisotropy indices of anhydrous Al-bearing orthopyroxene, those of hydrous Al-bearing

orthopyroxene seem higher, although the increase of D^{Vs} and A^{Vp} are too small to be considered significant. The A^{U} is most sensitive to the structural H_2O. 842-900 ppm H_2O increases the A^{U} by 14.4(30)%.

4. Discussion and Implications

Within the crystal structure of orthopyroxene, Si-O tetrahedra are connected by the bridging atom O3 to form chains extending along the c-axis, and the (Mg,Fe)-O octahedra are linked with each other through edge-shearing (Fig. S1). The M1 and M2 sites are at the centers of edge-sharing octahedron and discontinuous octahedron, respectively. Compared to Mg, Fe prefers occupying the slightly larger M2 site (Thompson and Downs, 2003). As suggested by Duffy and Vaughan (1988) and Bass and Weidner (1984) for anhydrous orthopyroxene, the C_{11}, C_{22} and C_{33} are controlled by the stiffness of the M1, M2 octahedra site and the compressibility of the Si-O tetrahedra chain, respectively. The shear elastic moduli C_{44}, C_{55}, and C_{66} are strongly affected by site ordering. Among them, C_{44} is more sensitive to composition and C_{55} and C_{66} are more sensitive to the octahedra stacking along *a*-axis. Finally, the off-diagonal elastic moduli C_{12}, C_{13}, and C_{23} vary slightly with either structure or composition. The substitution mechanism in hydrous orthopyroxene is dominated by the replacement of Si^{4+} with $Al^{3+} + H^{+}$ in the tetrahedral site or $Al^{3+} + H^{+}$ for 2 Mg^{2+} in the M1 site (Mierdel et al., 2007). The reduction of C_{11}, C_{22} and C_{33} caused by incorporation of 842-900 ppm structural H_2O is insignificant considering the uncertainty, suggesting that the substitution into the tetrahedral and octahedral sites does not induce a significant change in the compressibility along the a, b and c-axis. Among C_{44}, C_{55}, and C_{66}, C_{55} shows the least compositional variation (Duffy and Vaughan, 1988). This is consistent with our observed increase of C_{44} and C_{66} yet negligible change in C_{55} as shown in Figure 3. The changes of the off-diagonal C_{ij}s such as C_{12}, C_{13}, and C_{23} observed in this study is difficult to be explained structurally, possibly related to the complicated effect caused by both the substitution of Al^{3+} into the tetrahedral site and the vacancies in the octahedral M1 and M2 sites introduced by hydration (Hua et al., 2020). Measurements of orthopyroxene with higher H_2O concentrations may provide further insight into the hydrogen induced elasticity variations.

Although 842-900 ppm structural H_2O has limited effect on the single-crystal elasticity of

orthopyroxene, Mierdel et al. (2007) suggested that the incorporated structural H_2O could reach up to 0.8 wt.% in the Fe-bearing orthopyroxene with high Al_2O_3 contents. With such a high H_2O content, the subtle decrease of V_P and increase of D^{Vs} and A^{Vp} can be more significant. In addition, the incorporation of Al and H_2O in orthopyroxene has an important effect on the development of deformation fabrics, which enhances the Vp anisotropy significantly (Manthilake et al., 2013). Considering the extremely high heterogeneity in the Earth's upper mantle and lower crust, the hydration effect in terms of seismic anisotropy can be important in the lithologies that are enriched in orthopyroxene, e.g. orthopyroxenite and pyroxenite (Arai et al., 2006; Smith et al., 1999), although future measurements at high pressure-temperature conditions on orthopyroxene with higher H_2O concentrations are needed to better quantify this effect.

Author contributions: Conceptualization, J.S.Z. and M.Q.H.; Methodology, M.Q.H., W.Z., and M.H., Software and formal analysis, W.Z., M.H., and M.Q.H.; Sample synthesis: F.T.H. and J. K.; Sample orientation measurements: P. K. D. and D. Z.; Resources: J.S.Z; Writing-origin draft preparation: M.Q.H.; Writing-review and editing, J.S.Z. and everyone else; Visualization M.Q.H., W.Z., and M.H.; Project administration, J.S.Z.; Funding acquisition, J.S.Z.

Funding: This research was funded by NSF Grant EAR-1847707 (J.S.Z.) at the University of New Mexico. PD acknowledges support from NSF grant EAR-1722969.

Conflicts of interest: The authors declare no conflict of interest. The funders had no role in the design of the study, in the collection, analyses, or interpretation of data, in the writing of the manuscript, or in the decision to publish the results.

References

Arai, S., Shimizu, Y., Morishita, T., and Ishida, Y. (2006). A new type of orthopyroxenite xenolith from Takashima, Southwest Japan: silica enrichment of the mantle by evolved alkali basalt. Contributions to Mineralogy and Petrology, 152(3), 387.

Bass, J. D., and Weidner, D. J. (1984). Elasticity of single‐crystal orthoferrosilite. Journal of Geophysical Research: Solid Earth, 89(B6), 4359-4371.

Buchen, J., Marquardt, H., Speziale, S., Kawazoe, T., Ballaran, T. B., and Kurnosov, A. (2018). High-pressure single-crystal elasticity of wadsleyite and the seismic signature of water in the shallow transition zone. Earth and Planetary

297 Science Letters, 498, 77-87.
298 Chai, M., Brown, J. M., and Slutsky, L. J. (1997). The elastic constants of an aluminous orthopyroxene to 12.5 GPa.
299 Journal of Geophysical Research: Solid Earth, 102(B7), 14779-14785.
300 Costa, F., and Chakraborty, S. (2008). The effect of water on Si and O diffusion rates in olivine and implications for
301 transport properties and processes in the upper mantle. Physics of the Earth and Planetary Interiors, 166(1-2),
302 11-29.
303 Demouchy, S., and Bolfan-Casanova, N. (2016). Distribution and transport of hydrogen in the lithospheric mantle: A
304 review. Lithos, 240, 402-425.
305 Duffy, T. S., and Vaughan, M. T. (1988). Elasticity of enstatite and its relationship to crystal structure. Journal of
306 Geophysical Research: Solid Earth, 93(B1), 383-391.
307 Fan, D., Xu, J., Lu, C., Tkachev, S. N., Li, B., Ye, Z., et al. (2019). Elasticity of single-crystal low water content hydrous
308 pyrope at high-pressure and high-temperature conditions. American Mineralogist, 104(7), 1022-1031.
309 Flesch, L. M., Li, B., and Liebermann, R. C. (1998). Sound velocities of polycrystalline MgSiO 3-orthopyroxene to 10 GPa
310 at room temperature. American Mineralogist, 83(5-6), 444-450.
311 Grant, K. J., Kohn, S. C., and Brooker, R. A. (2006). Solubility and partitioning of water in synthetic forsterite and
312 enstatite in the system MgO–SiO 2–H 2 O±Al 2 O 3. Contributions to Mineralogy and Petrology, 151(6),
313 651-664.
314 Hill, R. (1963). Elastic properties of reinforced solids: some theoretical principles. Journal of the Mechanics and Physics
315 of Solids, 5, 357-372.
316 Hua, F. T.-S., Dera, P., and Kung, J. (2020). Compressional Behavior of Hydrous Orthoenstatite: Insight into the Nature of
317 LVZ under Continental Plate. Minerals, 10(1), 71.
318 Inoue, T., Weidner, D. J., Northrup, P. A., and Parise, J. B. (1998). Elastic properties of hydrous ringwoodite (γ-phase) in
319 Mg2SiO4. Earth and Planetary Science Letters, 160(1-2), 107-113.
320 Inoue, T., Yurimoto, H., and Kudoh, Y. (1995). Hydrous modified spinel, Mg1. 75SiH0. 5O4: a new water reservoir in the
321 mantle transition region. Geophysical Research Letters, 22(2), 117-120.
322 Jackson, J. M., Sinogeikin, S. V., and Bass, J. D. (1999). Elasticity of MgSiO3 orthoenstatite. American Mineralogist, 84(4),
323 677-680.
324 Jackson, J. M., Sinogeikin, S. V., and Bass, J. D. (2007). Sound velocities and single-crystal elasticity of orthoenstatite to
325 1073 K at ambient pressure. Physics of the Earth and Planetary Interiors, 161(1-2), 1-12.
326 Jacobsen, S. D., Jiang, F., Mao, Z., Duffy, T. S., Smyth, J. R., Holl, C. M., and Frost, D. J. (2008). Effects of hydration on the
327 elastic properties of olivine. Geophysical Research Letters, 35(14).
328 Jacobsen, S. D., Liu, Z., Ballaran, T. B., Littlefield, E. F., Ehm, L., and Hemley, R. J. (2010). Effect of H2O on upper mantle
329 phase transitions in MgSiO3: Is the depth of the seismic X-discontinuity an indicator of mantle water content?
330 Physics of the Earth and Planetary Interiors, 183(1-2), 234-244.
331 Kavner, A. (2003). Elasticity and strength of hydrous ringwoodite at high pressure. Earth and Planetary Science Letters,
332 214(3-4), 645-654.
333 Kohlstedt, D. L., Keppler, H., and Rubie, D. (1996). Solubility of water in the α, β and γ phases of (Mg, Fe) 2 SiO 4.
334 Contributions to Mineralogy and Petrology, 123(4), 345-357.
335 Kong, F., Gao, S. S., Liu, K. H., Ding, W., and Li, J. (2020). Slab Dehydration and Mantle Upwelling in the Vicinity of the
336 Sumatra Subduction Zone: Evidence from Receiver Function Imaging of Mantle Transition Zone Discontinuities.
337 Journal of Geophysical Research: Solid Earth, e2020JB019381.
338 Mans, W., Zhang, J. S., Hao, M., Smyth, J. R., Zhang, D., Finkelstein, G. J., and Dera, P. (2019). Hydrogen Effect on the
339 Sound Velocities of Upper Mantle Omphacite. Minerals, 9(11), 690.
340 Manthilake, M., Miyajima, N., Heidelbach, F., Soustelle, V., and Frost, D. J. (2013). The effect of aluminum and water on

the development of deformation fabrics of orthopyroxene. Contributions to Mineralogy and Petrology, 165(3), 495-505.

Mao, Z., Jacobsen, S., Jiang, F., Smyth, J., Holl, C., and Duffy, T. (2008). Elasticity of hydrous wadsleyite to 12 GPa: implications for Earth's transition zone. Geophysical Research Letters, 35(21).

Mao, Z., Jacobsen, S. D., Frost, D. J., McCammon, C. A., Hauri, E. H., and Duffy, T. S. (2011). Effect of hydration on the single-crystal elasticity of Fe-bearing wadsleyite to 12 GPa. American Mineralogist, 96(10), 1606-1612.

Mao, Z., Lin, J.-F., Jacobsen, S. D., Duffy, T. S., Chang, Y.-Y., Smyth, J. R., et al. (2012). Sound velocities of hydrous ringwoodite to 16 GPa and 673 K. Earth and Planetary Science Letters, 331, 112-119.

Mierdel, K., Keppler, H., Smyth, J. R., and Langenhorst, F. (2007). Water solubility in aluminous orthopyroxene and the origin of Earth's asthenosphere. Science, 315(5810), 364-368.

Musgrave, M. J. P. (1970). *Crystal acoustics: introduction to the study of elastic waves and vibrations in crystals*: (Holden-Day, San Francisco, 1970).

Ni, H., Zheng, Y.-F., Mao, Z., Wang, Q., Chen, R.-X., and Zhang, L. (2017). Distribution, cycling and impact of water in the Earth's interior. National Science Review, 4(6), 879-891.

Ohtani, E. (2005). Water in the mantle. Elements, 1(1), 25-30.

Ohtani, E. (2015). Hydrous minerals and the storage of water in the deep mantle. Chemical Geology, 418, 6-15.

Ohtani, E., Litasov, K., Hosoya, T., Kubo, T., and Kondo, T. (2004). Water transport into the deep mantle and formation of a hydrous transition zone. Physics of the Earth and Planetary Interiors, 143, 255-269.

Pearson, D., Brenker, F., Nestola, F., McNeill, J., Nasdala, L., Hutchison, M., et al. (2014). Hydrous mantle transition zone indicated by ringwoodite included within diamond. Nature, 507(7491), 221-224.

Perrillat, J. P., Nestola, F., Sinogeikin, S. V., and Bass, J. D. (2007). Single-crystal elastic properties of Ca0.07Mg1.93Si2O6 orthopyroxene. American Mineralogist, 92(1), 109-113.

Picek, S. M. (2015). Sound velocity study of natural orthopyroxenes with varying iron content. Master Thesis, University of Illinois at Urbana-Champaign, https://www.ideals.illinois.edu/handle/2142/78756.

Qian, W., Wang, W., Zou, F., and Wu, Z. (2018). Elasticity of orthoenstatite at high pressure and temperature: Implications for the origin of low VP/VS zones in the mantle wedge. Geophysical Research Letters, 45(2), 665-673.

Ranganathan, S. I., and Ostoja-Starzewski, M. (2008). Universal elastic anisotropy index. Physical Review Letters, 101(5), 055504.

Rauch, M., and Keppler, H. (2002). Water solubility in orthopyroxene. Contributions to Mineralogy and Petrology, 143(5), 525-536.

Reynard, B., Bass, J. D., and Brenizer, J. (2010). High-temperature elastic softening of orthopyroxene and seismic properties of the lithospheric upper mantle. Geophysical Journal International, 181(1), 557-566.

Sakurai, M., Tsujino, N., Sakuma, H., Kawamura, K., and Takahashi, E. (2014). Effects of Al content on water partitioning between orthopyroxene and olivine: Implications for lithosphere–asthenosphere boundary. Earth and Planetary Science Letters, 400, 284-291.

Schulze, K., Marquardt, H., Kawazoe, T., Ballaran, T. B., McCammon, C., Koch-Müller, M., et al. (2018). Seismically invisible water in Earth's transition zone? Earth and Planetary Science Letters, 498, 9-16.

Smith, D., Riter, J. A., and Mertzman, S. A. (1999). Water–rock interactions, orthopyroxene growth, and Si-enrichment in the mantle: evidence in xenoliths from the Colorado Plateau, southwestern United States. Earth and Planetary Science Letters, 165(1), 45-54.

Smyth, J. R., Mierdel, K., Keppler, H., Langenhorst, F., Dubrovinsky, L., and Nestola, F. (2007). Crystal chemistry of hydration in aluminous orthopyroxene. American Mineralogist, 92(5-6), 973-976.

Speziale, S., Marquardt, H., and Duffy, T. S. (2014). Brillouin scattering and its application in geosciences. Reviews in

Mineralogy and Geochemistry, 78(1), 543-603.

Thompson, R. M., and Downs, R. T. (2003). Model pyroxenes I: Ideal pyroxene topologies. American Mineralogist, 88(4), 653-666.

Van der Meijde, M., Marone, F., Giardini, D., and Van der Lee, S. (2003). Seismic evidence for water deep in Earth's upper mantle. Science, 300(5625), 1556-1558.

Webb, S. L., and Jackson, I. (1993). The pressure dependence of the elastic moduli of single-crystal orthopyroxene (Mg0. 8Fe0. 2) SiO3. European Journal of Mineralogy, 1111-1120.

Weidner, D. J., and Carleton, H. R. (1977). Elasticity of coesite. Journal of Geophysical Research: Solid Earth, 82(8), 1334-1346.

Whitfield, C. H., Brody, E. M., and Bassett, W. A. (1976). Elastic moduli of NaCl by Brillouin scattering at high pressure in a diamond anvil cell. Review of Scientific Instruments, 47(8), 942-947.

Xu, J., Zhang, D., Fan, D., Zhang, J. S., Hu, Y., Guo, X., et al. (2018). Phase transitions in orthoenstatite and subduction zone dynamics: Effects of water and transition metal ions. Journal of Geophysical Research: Solid Earth, 123(4), 2723-2737.

Yoshino, T., Matsuzaki, T., Shatskiy, A., and Katsura, T. (2009). The effect of water on the electrical conductivity of olivine aggregates and its implications for the electrical structure of the upper mantle. Earth and Planetary Science Letters, 288(1-2), 291-300.

Yuan, K., and Beghein, C. (2013). Seismic anisotropy changes across upper mantle phase transitions. Earth and Planetary Science Letters, 374, 132-144.

Zhang, B., Yoshino, T., Wu, X., Matsuzaki, T., Shan, S., and Katsura, T. (2012). Electrical conductivity of enstatite as a function of water content: implications for the electrical structure in the upper mantle. Earth and Planetary Science Letters, 357, 11-20.

Zhang, D., Jackson, J. M., Chen, B., Sturhahn, W., Zhao, J., Yan, J., and Caracas, R. (2013). Elasticity and lattice dynamics of enstatite at high pressure. Journal of Geophysical Research: Solid Earth, 118(8), 4071-4082.

Zhang, J. S., and Bass, J. D. (2016). Single‐crystal elasticity of natural Fe‐bearing orthoenstatite across a high‐pressure phase transition. Geophysical Research Letters, 43(16), 8473-8481.

Zhang, J. S., Bass, J. D., and Zhu, G. (2015). Single-crystal Brillouin spectroscopy with CO2 laser heating and variable q. Review of Scientific Instruments, 86(6), 063905.

This is the peer-reviewed, final accepted version for American Mineralogist, published by the Mineralogical Society of America.
The published version is subject to change. Cite as Authors (Year) Title. American Mineralogist, in press.
DOI: https://doi.org/10.2138/am-2021-7843. http://www.minsocam.org/

Figure captions

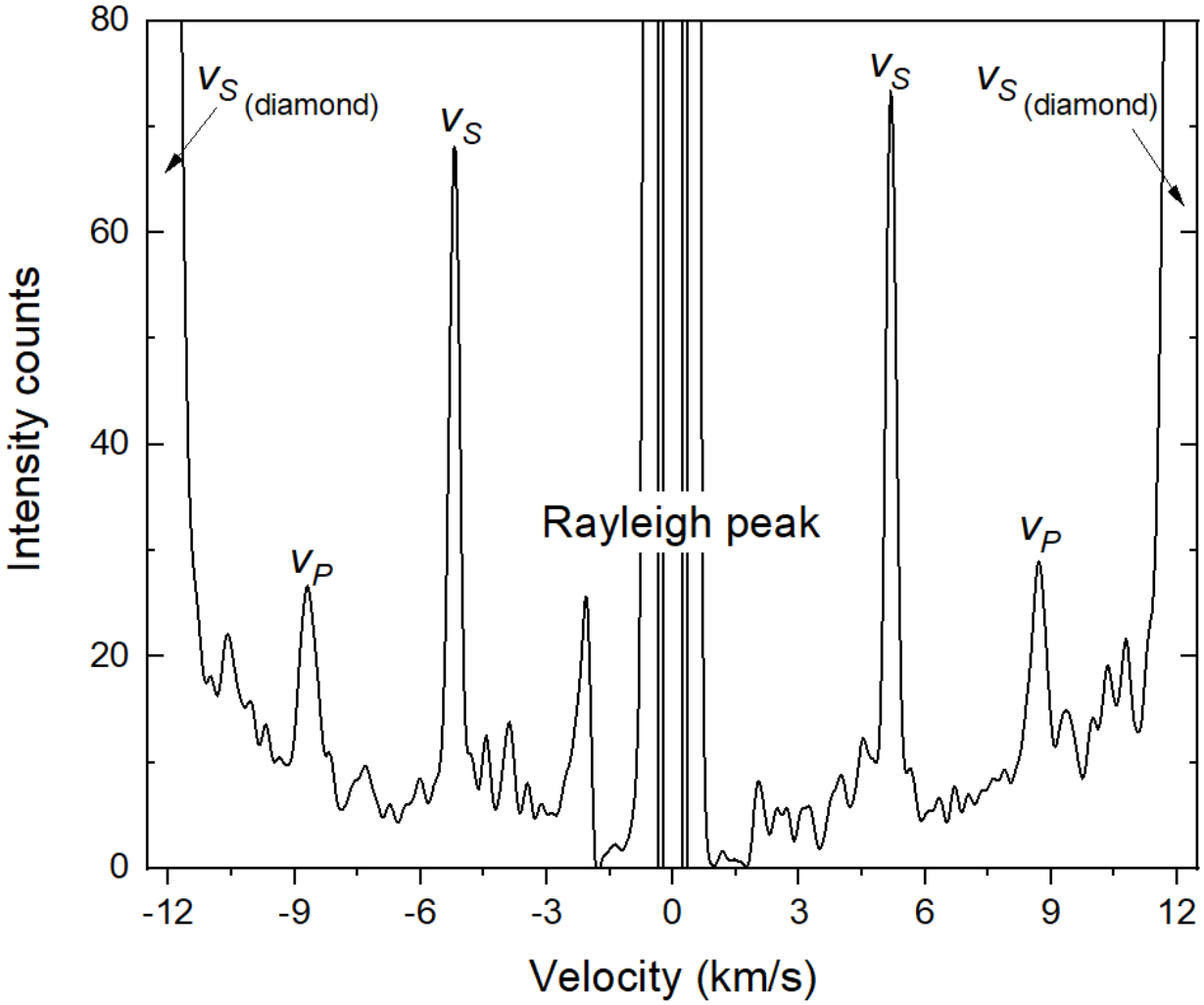

Figure 1. Representative Brillouin spectrum of the sample with plane normal (-0.566, 0.675, 0.472) measured at $\chi = 0^{\circ}$ for 10 minutes.

This is the peer-reviewed, final accepted version for American Mineralogist, published by the Mineralogical Society of America.
The published version is subject to change. Cite as Authors (Year) Title. American Mineralogist, in press.
DOI: https://doi.org/10.2138/am-2021-7843. http://www.minsocam.org/

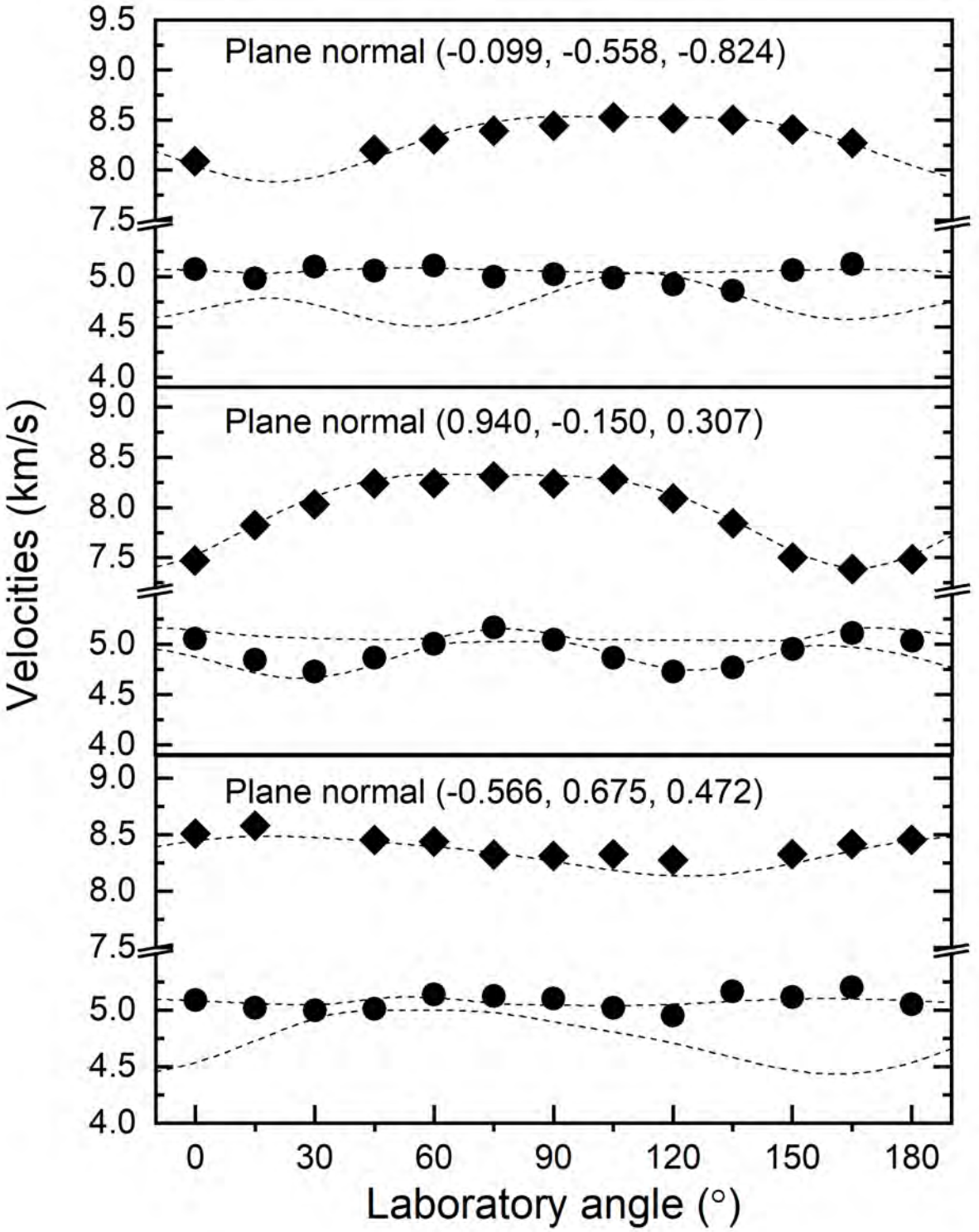

Figure 2. Acoustic velocities as a function of laboratory angle for the three hydrous Al-bearing orthopyroxene samples. The solid diamond and circle are measured v_P and v_S, respectively. Assigning the measured v_S as either v_{S1} or v_{S2} has negligible effect on the calculated C_{ij} model. The dashed curves are calculated from the best fit single-crystal C_{ij} model.

This is the peer-reviewed, final accepted version for American Mineralogist, published by the Mineralogical Society of America.
The published version is subject to change. Cite as Authors (Year) Title. American Mineralogist, in press.
DOI: https://doi.org/10.2138/am-2021-7843. http://www.minsocam.org/

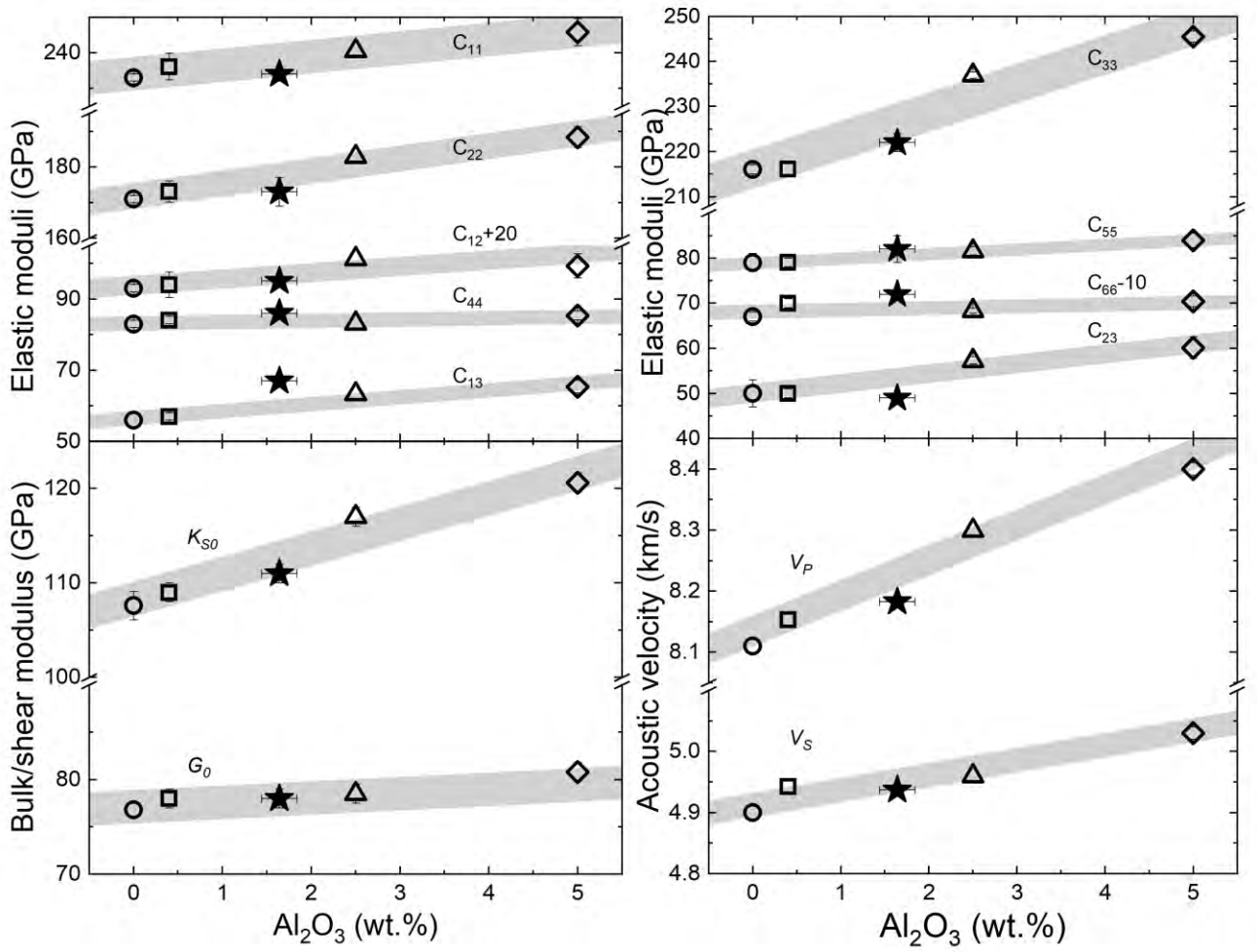

Figure 3. The effect of structural H_2O on the elasticity of orthopyroxene. The open circle, rectangle, triangle, and diamond symbols represent the elastic properties of anhydrous Al-bearing orthopyroxenes from Jackson et al. (1999), Jackson et al. (2007), Zhang and Bass (2016), and Chai et al. (1997), respectively, after removing the Fe and Ca effects according to Picek (2015) and Perrillat et al. (2007). The shaded areas are bounded by the 95% confidence interval after linear-fitting. The solid star represents the data of hydrous Al-bearing orthopyroxene determined in this study. Most error bars are smaller than the symbols.

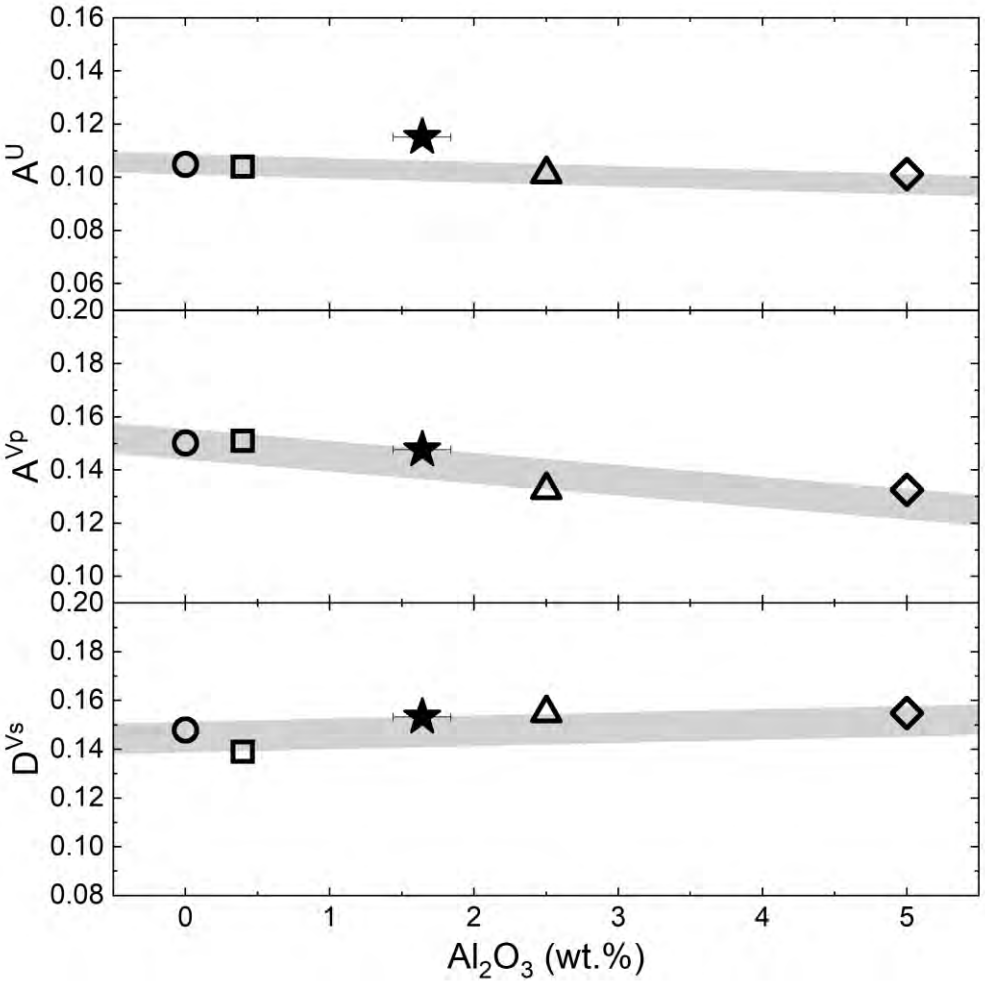

Figure 4. The effect of structural water on the A^U, A^{Vp}, and D^{Vs} of orthopyroxene. The symbols are the same as those in Figure 3.

436 Table 1. The effect of chemical impurities on the elasticity of $MgSiO_3$ orthopyroxene.
437

	Hydrous Al-bearing Orthopyroxene (this study)	Al,Fe,Ca-bearing Orthopyroxene (Zhang and Bass, 2016)	Al,Fe,Ca-bearing Orthopyroxene (Chai et al., 1997)	Al,Fe-bearing Orthopyroxene (Jackson et al., 2007)	Ca-bearing Orthopyroxene (Perrillat et al., 2007)	End-member Orthopyroxene(Jackson et al., 1999)
H_2O (ppm)	842-900	-	-	-	0	0
Fe#	0	8.4	9.5	0.2	0	0
Al_2O_3 (wt. %)	1.64	2.5	5.0	0.4	0	0
CaO (wt. %)	0	1.1	1.1	0	1.9	0
C_{11} (GPa)	235(2)	232.2(5)	236.9(10)	236(1)	224.1(1)	233(1)
C_{22} (GPa)	173(2)	175.7(7)	180.5(8)	173(1)	165.8(2)	171(1)
C_{33} (GPa)	222(2)	222.9(6)	230.4(10)	216(1)	202.9(1)	216(1)
C_{44} (GPa)	86(1)	82.2(4)	84.3(12)	84(1)	82.2(1)	83(1)
C_{55} (GPa)	82(1)	77.3(3)	79.4(8)	79(1)	73.8(1)	79(1)
C_{66} (GPa)	82(1)	78.1(6)	80.1(12)	80(1)	77.1(1)	77(1)
C_{12} (GPa)	75(3)	79.5(9)	79.6(16)	74(1)	71.4(1)	73(2)
C_{13} (GPa)	67(2)	61.2(6)	63.2(18)	57(1)	52.7(1)	56(2)
C_{23} (GPa)	49(2)	54.1(8)	56.8(24)	50(1)	45.2(1)	50(3)
ρ (g/cm^3)	3.218	3.288(4)	3.304	3.196(4)	3.209	3.194(6)
$K_{S,Voigt}$ (GPa)	112(1)	113(1)	116.3(5)	109.5(15)	103.5(15)	108.7(15)
$G_{S,Voigt}$ (GPa)	79.1(5)	76.6(7)	78.6(4)	78.6(7)	74.9(11)	77.2(7)
$K_{S,Reuss}$ (GPa)	110(1)	112(1)	114.6(5)	107.4(15)	101.5(15)	106.7(15)

This is the peer-reviewed, final accepted version for American Mineralogist, published by the Mineralogical Society of America.
The published version is subject to change. Cite as Authors (Year) Title. American Mineralogist, in press.
DOI: https://doi.org/10.2138/am-2021-7843. http://www.minsocam.org/

$G_{S,\mathrm{Reuss}}$ (GPa)	77.7(5)	75.2(7)	77.3(4)	77.3(7)	73.5(11)	75.9(7)
$K_{S,\mathrm{VRH}}$ (GPa)	111(2)	113(1)	115.5(5)	108.5(15)	102.5(15)	107.6(15)
$G_{S,\mathrm{VRH}}$ (GPa)	78.4(1)	75.9(7)	78.1(4)	77.9(7)	74.2(11)	76.8(7)
V_P (km/s)	8.18(3)	8.06(3)	8.15(1)	8.15(8)	7.92	8.11
V_S (km/s)	4.94(2)	4.80(2)	4.86(1)	4.94(5)	4.81	4.90

438